Journal of Rock Mechanics and Geotechnical Engineering 14 (2022) 460–476

Contents lists available at ScienceDirect

Journal of Rock Mechanics and Geotechnical Engineering

journal homepage: www.jrmge.cn

Full Length Article

Mechanical behaviours of sandstone containing intersecting fissures under uniaxial compression

Fei Xiong [a,b,c,d], Xinrong Liu [a,b,c,*], Xiaohan Zhou [a,b,c,**], Guangyi Lin [a], Dongshuang Liu [a], Yafeng Han [a], Bin Xu [a], Chunmei He [e], Zijuan Wang [f]

[a] School of Civil Engineering, Chongqing University, Chongqing, 400045, China
[b] State Key Laboratory of Coal Mine Disaster Dynamics and Control, Chongqing University, Chongqing, 400044, China
[c] National Joint Engineering Research Center of Geohazards Prevention in the Reservoir Areas, Chongqing University, Chongqing, 400045, China
[d] State Key Laboratory for Geomechanics and Deep Underground Engineering, China University of Mining and Technology, Xuzhou, 221116, China
[e] College of Architectural Engineering, Neijiang Normal University, Neijiang, 641100, China
[f] School of Management Science and Engineering, Chongqing Technology and Business University, Chongqing, 400067, China

ARTICLE INFO

Article history:
Received 21 February 2021
Received in revised form
20 July 2021
Accepted 9 September 2021
Available online 18 November 2021

Keywords:
Intersecting fissures
Sandstone
Uniaxial compression
Fracture determination
Cracking evolution

ABSTRACT

Predicting rock cracking is important for assessing the stability of underground engineering. The effects of the intersecting angle α and the distribution orientation angle β of intersecting fissures on the uniaxial compressive strength and the failure characteristics of sandstone containing intersecting fissures are investigated through laboratory experiments and two-dimensional particle flow code (PFC2D). The relationship between the mechanical properties of sandstone and the intersecting angle α and the distribution orientation angle β is analysed. Crack initiation forms and the final failure modes are then categorised and determined via empirical methods. In addition, the cracking processes of intersecting fissures with different α and β values are discussed. The results show that variations in the peak stress, peak strain, average modulus, and crack initiation stress of sandstone containing intersecting fissures show a "moth" shape in the space of the α-β-mechanical parameters. Two crack initiation forms are identified: inner tip cracking (usually accompanied by one outer tip cracking) and only outer tips cracking. Two failure modes are observed: (1) the main fracture planes are created at the inner tip and one outer tip, and (2) the main fracture planes are formed at the two outer tips. Two main crack evolution processes of sandstone containing intersecting fissures under uniaxial compression are found. Approaches for quickly determining the crack initiation form and the failure mode are proposed. The combination of the determination equations for the crack initiation form and the failure mode can be used to predict the crack evolution. The approach for determining the crack evolution processes is hence proposed with acceptable precision.

© 2022 Institute of Rock and Soil Mechanics, Chinese Academy of Sciences. Production and hosting by Elsevier B.V. This is an open access article under the CC BY-NC-ND license (http://creativecommons.org/licenses/by-nc-nd/4.0/).

1. Introduction

As a complex geological body, rocks contain many discontinuities in various forms (Yin et al., 2018; Liu et al., 2019; Romer and Ferentinou, 2019; Shaunik and Singh, 2019; Han et al., 2020; Cui and Gratchev, 2020). For example, intersecting fissures are common in natural rock, as shown in Brideau et al. (2009) in Fig. 1. The angle between the two fissures is α, and the angle between the angle bisector of the two fissures and the horizontal direction is β (distribution orientation angle). The mechanical behavior of rock masses is greatly influenced by the geometrical characteristics of fissures. New cracks form at the tips of pre-existing fissures when an external force is applied. The propagation of new cracks leads to the destruction and instability of the engineering rock mass. Current research focuses on discrete and intermittent single cracks (Wong and Einstein, 2009a; Yang and Jing, 2011), double cracks (Wong and Chau, 1998; Wong and Li, 2013), triple cracks (Cao et al., 2015; Zhang et al., 2019), or cracks in groups (Sagong and Bobet, 2002; Prudencio and Jan 2007). However, there is an insufficient study on the crack evolution characteristics of intersecting fissures.

* Corresponding author. School of Civil Engineering, Chongqing University, Chongqing, 400045, China.
** Corresponding author. School of Civil Engineering, Chongqing University, Chongqing, 400045, China.
E-mail addresses: liuxrong@126.com (X. Liu), zhouxh2008@126.com (X. Zhou).
Peer review under responsibility of Institute of Rock and Soil Mechanics, Chinese Academy of Sciences.

https://doi.org/10.1016/j.jrmge.2021.09.008
1674-7755 © 2022 Institute of Rock and Soil Mechanics, Chinese Academy of Sciences. Production and hosting by Elsevier B.V. This is an open access article under the CC BY-NC-ND license (http://creativecommons.org/licenses/by-nc-nd/4.0/).

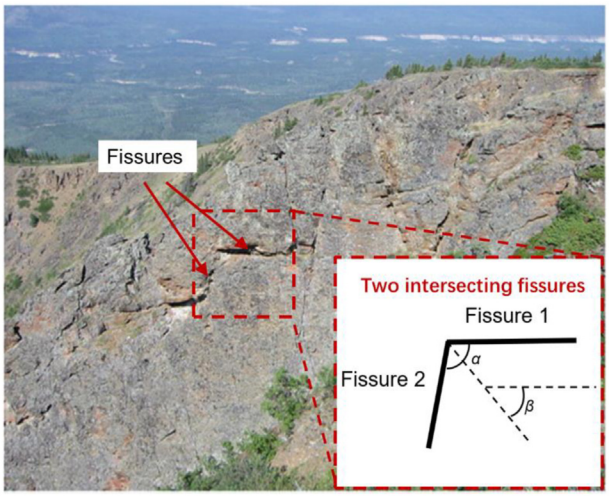

Fig. 1. Two intersecting fissures in a rock mass (Brideau et al., 2009).

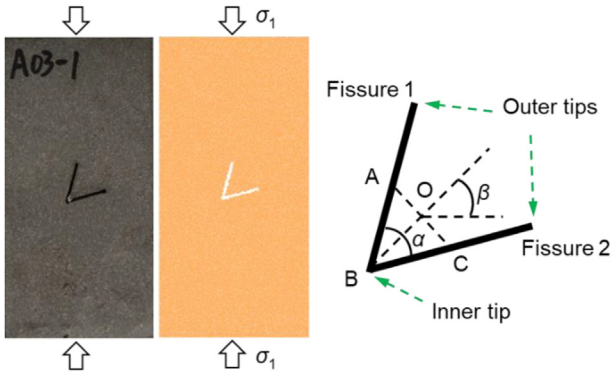

Fig. 2. The intersecting fissures in the samples.

Therefore, in-depth research into the mechanical behaviour of rock with intersecting fissures has excellent significance.

To better understand the instability and failure mechanisms of rocks, scholars have conducted extensive experimental studies. The effect of crack distribution forms in parallel (Bobet and Einstein, 1998; Wong and Chau, 1998; Cao et al., 2016; Zhao and Zhou, 2016; Liu et al., 2017, 2018; Feng et al., 2018a,b), nonparallel (Afolagboye et al., 2017; Feng et al., 2018c, 2019, 2020), coplanar (Wong and Einstein, 2009b,c; Wong and Li, 2013), and random (Haeri et al., 2014) on cracking behaviour has received substantial attention. Cracks form and propagate from the tips of the prefabricated fissure under uniaxial compression. The failure mode of the rock is determined by the fissure length and inclination angle (Yang and Jing, 2011). Cracks generated at fissure tips are divided mainly into tensile cracks, shear cracks, and mixed tensile-shear cracks (Wong and Einstein, 2009a). The coalescence behaviour between fissures is complex. In addition to stress conditions, the fissure angle, rock bridge inclination, fissure number, and fissure spacing affect the coalescence characteristics (Wang et al., 2017; Xu and Li, 2019). Meanwhile, the friction coefficient of the fissure surface also plays a key role (Park and Bobet, 2009). The pattern of coalescence between cracks is judged mainly by the types of coalescence cracks. For example, the coalescence categories between double fissures can be divided into eleven modes according to the coalescence crack types (Wong and Einstein, 2009b; Zhang and Wong, 2012). According to the coalescence crack types, Sagong and Bobet (2002) classified multiple fissure coalescence categories in gypsum samples into nine modes.

Table 1
Specific cases for the tested sandstone samples containing two intersecting fissures.

Case No.	a (mm)	α (°)	β (°)	Note
W-1				Intact samples
W-2				
#A06-1	20	30	45	Fissured samples
#A06-2	20	30	45	
#A06-3	20	30	45	
#A03-1	20	60	45	
#A03-2	20	60	45	
#A07-1	20	90	45	
#A07-2	20	90	45	
#A08-1	20	120	45	
#A08-2	20	120	45	
#A09-1	20	150	45	
#A09-2	20	150	45	

In addition to physical testing, many numerical methods have played an important role in the study of rock ruptures, such as the finite element method (FEM) (Bocca et al., 1990), the extended finite element method (XFEM) (Rozycki et al., 2008), the boundary element method (BEM) (Hosseini-Tehrani et al., 2005), and the discrete element method (DEM) (Scholtes and Donze, 2013; Liakas et al., 2017; Zhu et al., 2021). Among these methods, the DEM has been widely applied in research on rock fractures and crack propagation in rock materials under loading conditions (Zhang and Wong, 2012; Zhang et al., 2017; Feng et al., 2018c). However, the following limitations of DEM are unavoidable (Donze et al., 2009): (a) the elements size has a significant impact on the fracture, i.e. the size effect; (b) the cross effect exists due to the size and shape differences between elements with real grains; and (c) data from classical geotechnical tests that may be impractical are utilized to determine the link between the local and macroscopic constitutive laws. Even so, the DEM approach can directly and efficiently model microfracture and macrocrack propagation through bond breakage between particles instead of applying fracture mechanics theories related to the stress intensity factor for the fissure tip (Potyondy and Cundall, 2004). Particle flow code (PFC) has been demonstrated to effectively reproduce the process of crack initiation, propagation, and coalescence in extensive studies, with good agreement with experimental results (Lee and Jeon, 2011; Ghazvinian et al., 2012; Manouchehrian et al., 2014; Shi et al., 2018; Castro-Filgueira et al., 2020; Zhou et al., 2021).

Experimental studies and numerical simulations indicate that the geometrical characteristics of fissures have an important influence on the mechanical behaviour of rocks (Yang et al., 2017; Wang et al., 2019). Previous investigations have improved the understanding of complex fracture evolution in fractured rock. However, the major concern is given to intermittent fissures in different geometric forms, and less attention is given to intersecting fissures. For intersecting fissures, the intersecting angle between the fissures and the distribution orientation angle are unquestionably important geometrical parameters, of which the influence on the mechanical behaviours of sandstone is not clear.

On the above basis, the effects of the intersecting angle α and the distribution orientation angle β of intersecting fissures on the mechanical behaviour of sandstone under uniaxial compression were investigated via laboratory tests and discrete element simulations (i.e. two-dimensional particle flow code, PFC2D) in this paper. First, uniaxial compression tests on sandstone with intersecting fissures were conducted in the physical experiment. According to the macroscopic mechanical parameters of the

Table 2
Specific cases of intersecting fissures in the numerical simulation.

Case No.	a (mm)	α (°)	β (°)
#1	20	30	0, 30, 45, 60, 90
#2	20	60	0, 30, 45, 60, 90
#3	20	90	0, 30, 45, 60, 90
#4	20	120	0, 30, 45, 60, 90
#5	20	150	0, 30, 45, 60, 90

sandstone samples in the laboratory tests, the microscopic numerical parameters of the simulated sandstone were calibrated and verified. Then, the parameters were used to simulate uniaxial compression on sandstones containing intersecting fissures. The effects of α and β on the mechanical and failure properties of sandstone were thoroughly studied. The crack initiation form and failure mode of sandstone were analysed and predicted by the empirical approach. Finally, the cracking processes of samples with different α and β values were discussed and summarised. Approaches for determining the crack initiation form, the failure mode, and the crack evolution processes were then proposed.

2. Methodology

2.1. Intersecting fissures

All geometric parameters of the intersecting fissures studied include the length of Fissure 1, the length of Fissure 2, the intersecting angle α, and the distribution orientation angle β (see Fig. 1). The impact of the flaw length on the mechanical behaviour of fissured rock has been fully studied (Yang and Jing, 2011; Sun et al., 2019; Zhang et al., 2019). Therefore, the lengths of Fissures 1 and 2 are not of concern and these lengths were set to a constant value in this investigation. Referring to the lengths of fissures in the available literature (Yang et al., 2015; Feng et al., 2018 a,b, 2020; Zhang et al., 2019), the lengths of the two fissures are fixed to 20 mm. The fissure opening, which is controlled by the prefabrication method, is set to 1.8 mm, which is close to the value from the available literature (Yang and Jing, 2011; Yang et al., 2015; Zhang et al., 2017). The intersecting angle α between fissures and the distribution orientation angle β, two key geometrical parameters of the intersecting fissures, are the focus of this paper. Fig. 2 presents two intersecting fissures (Fissures 1 and 2, clockwise) in sandstone and numerical samples in this study. Both fissures have a length a of 20 mm and an opening of 1.8 mm. The midpoint O of line AC connecting the midpoints of the two fissures is located at the sample centre. The angle between two fissures is α, and the angle between the BO and the horizontal line is β. The geometric configurations of the intersecting fissures are thus controlled by α and β. The case of the sample containing the intersecting fissures is described by α and β, i.e. "sample α-β". For instance, "sample 30-0" means that the sample contains intersecting fissures with $\alpha = 30°$ and $\beta = 0°$. Hereafter, the term "fissure" represents pre-existing artificial flaws, while the term "crack" indicates newly generated flaws.

2.2. Experimental setups

Sandstone materials, which are common in stratum structures, were selected as the research objects in the experiment (Xiong et al., 2021). The sandstone was taken from Linyi, Shandong Province, China, with a density of 2441 kg/m^3. The fresh rock is dark red in the natural state, with uniform particles and no visible texture on the surface, and the mineral components are mainly quartz and feldspar.

Table 3
The microparameters used in the PFC2D model for sandstone.

Micro-parameter	Unit	Value
Minimum particle radius, r_{min}	mm	0.3
Ratio of particle radius, r_{max}/r_{min}		1.6
Effective parallel-bond modulus, $\overline{E_c}$	GPa	1
Ratio of normal to shear stiffness of the parallel bond, $\overline{k_n}/\overline{k_s}$		1.3
Tensile strength of the parallel bond, σ_c	MPa	14.6
Cohesion of the parallel bond, c	MPa	15.8
Friction angle of the parallel bond, φ	°	46

The collected sandstone was cut and polished to form a rectangular parallelepiped sample with height, width and thickness of 160 mm, 80 mm and 30 mm, respectively. A high-pressure water jet cutting machine was used to prefabricate two intersecting fissures in the sample. During fissure processing, the water pressure of the high-pressure water jet cutting machine was kept constant to reduce the influence of the change in the fissure opening on the test results (Xiong et al., 2021).

Sandstone samples were subjected to uniaxial compression tests on a YNS-2000 electrohydraulic servo-controlled test system. This test system has a high level of triple closed-loop control technology, which can realise the closed-loop control of force, deformation, and displacement. Consisting of a loading frame and a data acquisition system, the loading frame has a 2000 kN load capacity, and the axial load and deformation can be recorded simultaneously by the data acquisition system. The displacement load mode was employed during the experiment with a loading rate of 0.0017 mm/s. To decrease the friction effect between the sample end and the load frame, petroleum jelly was applied to the upper and lower ends of the sample. During uniaxial compression, a Sony HDR-CX900E video camera was used to monitor the cracking processes of fissured samples with images taken at a frame rate of 25 fps. The resolution of each frame in the video was 1920 × 1080 pixels, covering the representative area of the surface of a fissured sample at a resolution of approximately 420 pixels in width and 840 pixels in height. The specific cases for intersecting fissures in laboratory tests are detailed in Table 1. The angle β is set at 45°, while α is increased from 30° to 150°, with an interval of 30°.

2.3. Numerical simulation

2.3.1. Simulation method

The uniaxial compression tests for sandstone samples with intersecting fissures were simulated using PFC2D. There are two common models in PFC, i.e. the contact bond model and parallel bond model. The contact bond model can transfer only forces, while the parallel bond model can transfer both forces and moments. Therefore, the parallel bond model, which can better simulate rock materials, was adopted. The size of the numerical sample is the same as that of the experimental sample, with a width of 80 mm and a height of 160 mm. The particle radius of the model is uniformly distributed in the range of 0.3–0.48 mm, which is appropriate for simulating sandstone materials (Bahaaddini et al., 2014; Yang et al., 2015; Cheng et al., 2016). The established intact numerical sandstone sample contains 26,023 particles and 75,174 contacts. Two intersecting fissures were established by deleting particles in the sample, as shown in Fig. 2.

Uniaxial compression was performed by applying an axially downward displacement load on the top end of the sample. For the loading speed, Zhang and Wong (2013) believed that the acceptable static loading in PFC2D has an upper limit of 0.08 m/s. To ensure static loading, the loading rate was set to 0.05 m/s. The specific

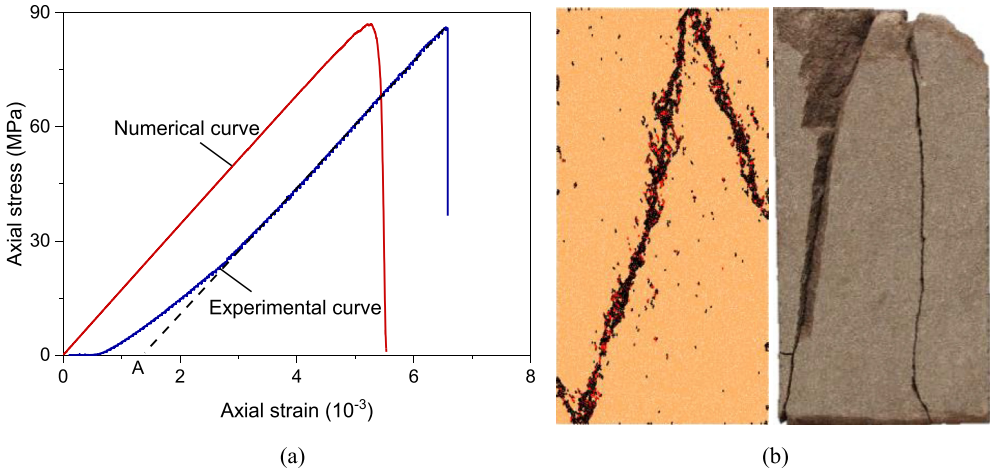

Fig. 3. Comparison between the experimental and numerical results of an intact sandstone sample under uniaxial compression (Xiong et al., 2017, 2021): (a) Axial stress–strain curves and (b) Final failure modes.

Table 4
Comparison between the experimental and numerical mechanical parameters for intact sandstone.

Mechanical parameter	Unit	Experimental value	Numerical value
Density	kg/m^3	2441	2441
Uniaxial compressive strength	MPa	86.18	87.04
Average modulus	GPa	16.93	17.13

cases for intersecting fissures in the numerical simulation are detailed in Table 2.

2.3.2. Parameter calibration

The macroscopic properties of the material are determined by the microparameters in PFC2D. As a result, establishing a relationship between the microparameters and the macroparameters in PFC is critical. Based on the results of previous PFC simulations (Huang and Zhu, 2018; Shi et al., 2018; Zhang et al., 2021), the effective parallel-bond modulus, parallel-bond tensile strength, cohesion, friction angle, and ratio of normal to shear stiffness have significant influences on the mechanical charactristics. Therefore, a calibration was performed to select reasonable values for these microparameters. The elastic modulus is greatly affected by the effective parallel-bond modulus. Poisson's ratio is largely determined by the ratio of the normal to shear stiffness of the parallel bond, and the tensile and shear strengths of the parallel bond significantly affect the compressive strength and tensile strength. When the tensile stress of the parallel bond exceeds its tensile strength, the bond breaks in tension, while if the shear strength of the bond is exceeded, the bond is broken in shear.

Directly determining the microscopic parameters that match the experimental results in PFC is difficult. Hence, the trial and error method was used to calibrate the microparameters. The numerical results obtained after each trial of uniaxial compression simulation were checked using the experimental results. This process was repeated until the numerical results matched the experimental results well. By this method, a set of reasonable microparameters of the sandstone was obtained, as shown in Table 3. To examine the reasonability of these numerical microparameters, macroparameters and macrofailure patterns were used for comparison. Fig. 3 depicts the axial stress–strain curve and failure mode of the intact numerical sandstone sample under uniaxial compression. The results of the experimental sample in the reference (Xiong et al., 2017, 2021) are also given for comparison. Fig. 3a indicates that the stress–strain curves of the numerical sample and the experimental sandstone sample are essentially consistent, including the elastic stage, the prepeak stage, and postpeak failure. The experimental and numerical curves both drop rapidly after the peak, showing the brittleness of the sandstone. The initial nonlinear deformation appears in the experimental sample at a low stress due to the closure of the primary cracks, which are not observed in the numerical results. From Fig. 3b, the failure modes of the numerical and experimental samples both exhibit splitting failure, and the main fracture plane is essentially created in the axial direction, showing a good consistency between the experiment and numerical simulations. Table 4 gives the mechanical parameters of the numerical and experimental samples, which shows that the error of the peak stress and the average modulus is within 1.18%. The above comparisons calibrate the correctness and rationality of the microscopic parameters in Table 3.

3. Comparison between the experimental and numerical results

To further verify the applicability of the calibrated parameters to the sandstone samples with intersecting fissures, the simulated results of sandstone samples containing intersecting fissures with $\beta = 45°$ and α varying from 30° to 150° were compared with the experimental results. Some of the experimental results utilized for comparison are obtained from the references (Xiong et al., 2017, 2021).

3.1. Strength and deformation characteristics

Fig. 4 shows the comparison between the experimental and numerical axial stress–strain curves of samples containing intersecting fissures with α varying from 30° to 150° at $\beta = 45°$ under uniaxial compression. Without considering the initial nonlinear deformation in the experimental curves, the numerical stress–strain curves resemble the experimental results. All the samples showed an obvious brittleness, and the stress dropped rapidly after the peak.

The experimental and numerical mechanical parameters are compared in Fig. 5. Fig. 5a and b shows that when $\beta = 45°$, the peak stress and the average modulus decrease with increasing α, and the simulated values show the same trend as the experimental values. Moreover, the simulated value is nearly identical to the

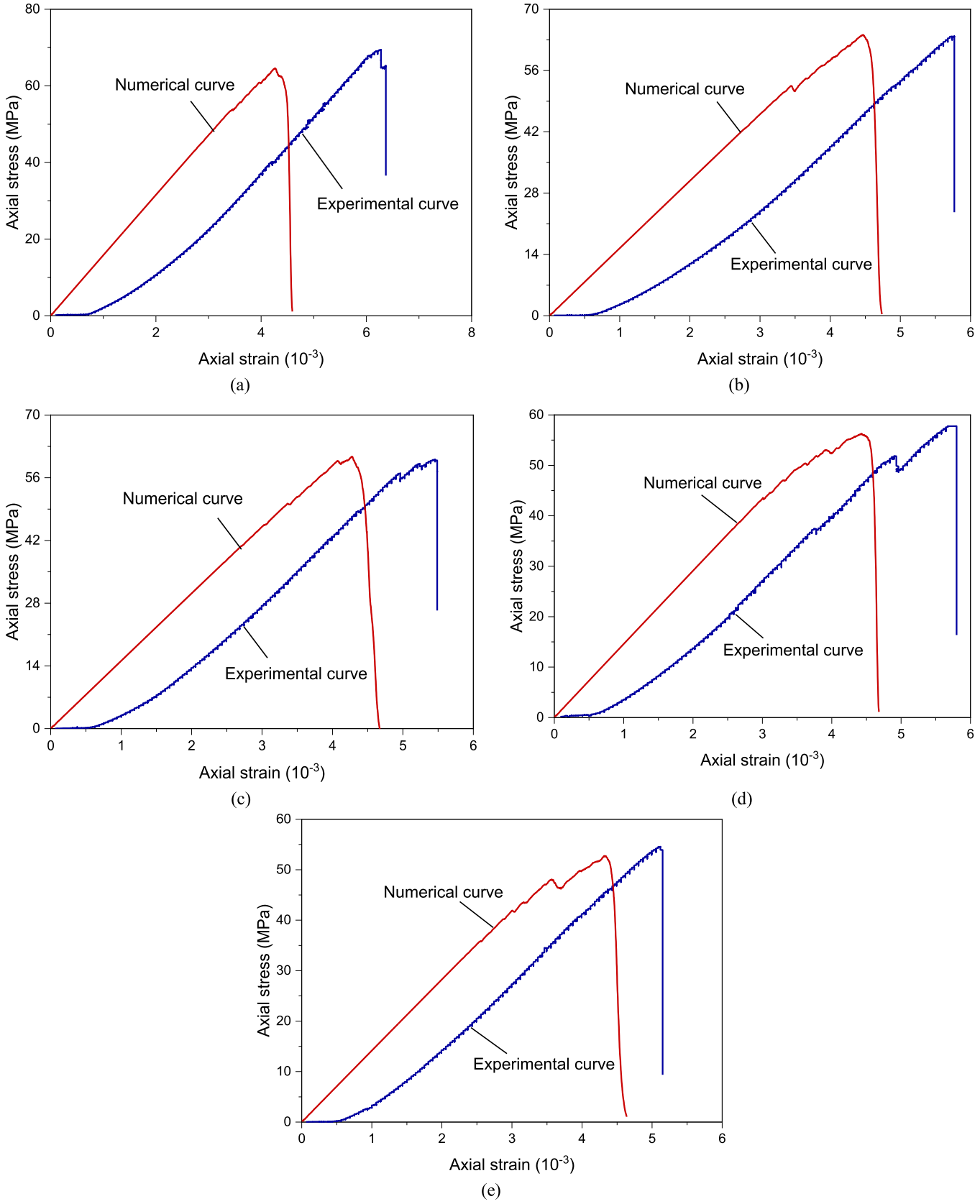

Fig. 4. Comparison between the experimental and numerical axial stress–strain curves of sandstone samples containing intersecting fissures with different α at $\beta = 45°$ under uniaxial compression: (a) $\alpha = 30°$, (b) $\alpha = 60°$, (c) $\alpha = 90°$, (d) $\alpha = 120°$, and (e) $\alpha = 150°$.

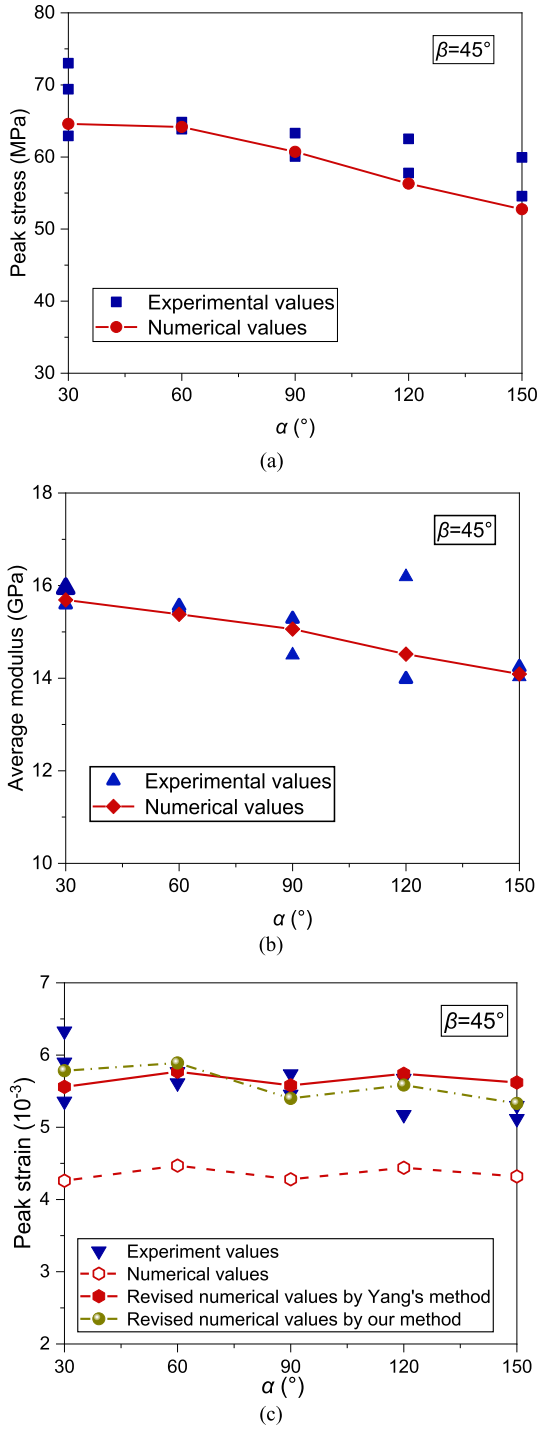

Fig. 5. Comparison between the experimental and numerical mechanical parameters of sandstone samples containing intersecting fissures, with α varying from 30° to 150° at $\beta = 45°$ under uniaxial compression: (a) Peak stress, (b) Average modulus, and (c) Peak strain.

experimental value for the same α. With an increase in α, the span of the intersecting fissures increases, resulting in a decrease in the effective bearing width of the samples, hence leading to a decrease in the strength. When α exceeds 90°, the experimental peak stresses are slightly higher than the numerical results, which may be caused by the following three reasons: (1) the three-dimensional (3D) experimental models cannot be accurately simulated by 2D numerical models. (Lee and Jeon, 2011); (2) the

Table 5
The average initial strain value of the experimental samples.

Sample	Average initial strain value
Intact	1.3
#A06 (30–45)	1.52
#A03 (60-45)	1.42
#A07 (90-45)	1.12
#A08 (120-45)	1.15
#A09 (150-45)	1.01

effect of the heterogeneity of the tested rock material or the intrinsic randomness of the numerical simulation (Yang et al., 2014); and (3) the slight differences in fissure sizes between experimental and numerical samples. By the fissure geometry form, when α exceeds 90°, the projection width of two intersecting fissures in the horizontal direction increases significantly, resulting in a sudden decrease in the effective bearing width of the samples. This sudden decrease in the effective bearing width amplifies the above three effects. Hence, the experimental peak stresses are different from the numerical results when α is equal to 120° and 150°. However, the errors between the simulated and experimental peak stresses are 6.39% at $\alpha = 120°$ and 7.85% at $\alpha = 150°$, which is acceptable.

Fig. 5c illustrates the comparison between the experimental and numerical peak strains of sandstone containing two intersecting fissures under uniaxial compression. Generally, the peak strain in the experiment is higher than the simulated value due to the initial nonlinear deformation in the experimental samples. Yang et al. (2014) revised the numerical peak strain by adding the initial strain value of the intact sample, obtaining better results. The same revision method was adopted to revise the numerical peak strain in this study, with the corresponding revised numerical peak strains given in Fig. 5c. From the figure, when α is equal to or smaller than 120°, the revised numerical peak strain is nearly identical to the experimental peak strain for the same α. However, as $\alpha = 150°$, the revised numerical peak strain (5.62×10^{-3}) is slightly higher (by 7.3%) than the experimental peak strain (5.21×10^{-3} for the average peak strain). The initial strain values of the experimental samples containing intersecting fissures vary with α, as shown in Table 5, which presents the average initial strain for different α values at $\beta = 45°$. We find that the average initial strain decreases with increasing α. These average initial strains for the samples with different α values are employed to revise the corresponding numerical peak strain, and the results are also plotted in Fig. 5c. Clearly, the revised numerical peak strain obtained by this method is approximately equal to the values obtained by the experiment for the same α. Moreover, the revised peak strains obtained by this method are close to those obtained by the method of Yang et al. (2014) for the same α, and the error is within 5.16%. Therefore, both methods are available and reasonable for revising the peak strain.

3.2. Final failure mode

Fig. 6 shows the variation in the failure modes of the experimental and numerical samples with varied α values at $\beta = 45°$. Due to the heterogeneity of the experimental sandstone, more macrocracks are created after failure. The main cracks are created at the fissure tips and form the main fracture planes (i.e. the main macrocracks that lead to the final unstable failure of the sample) in both the numerical and experimental samples. In general, the main fracture planes develop from tensile wing cracks or anti-wing cracks. The position of the main fracture plane depends on α. When $\alpha = 30°$ and 60°, cracks are generated at the inner and outer tips of Fissure 2, forming two main fracture planes. The

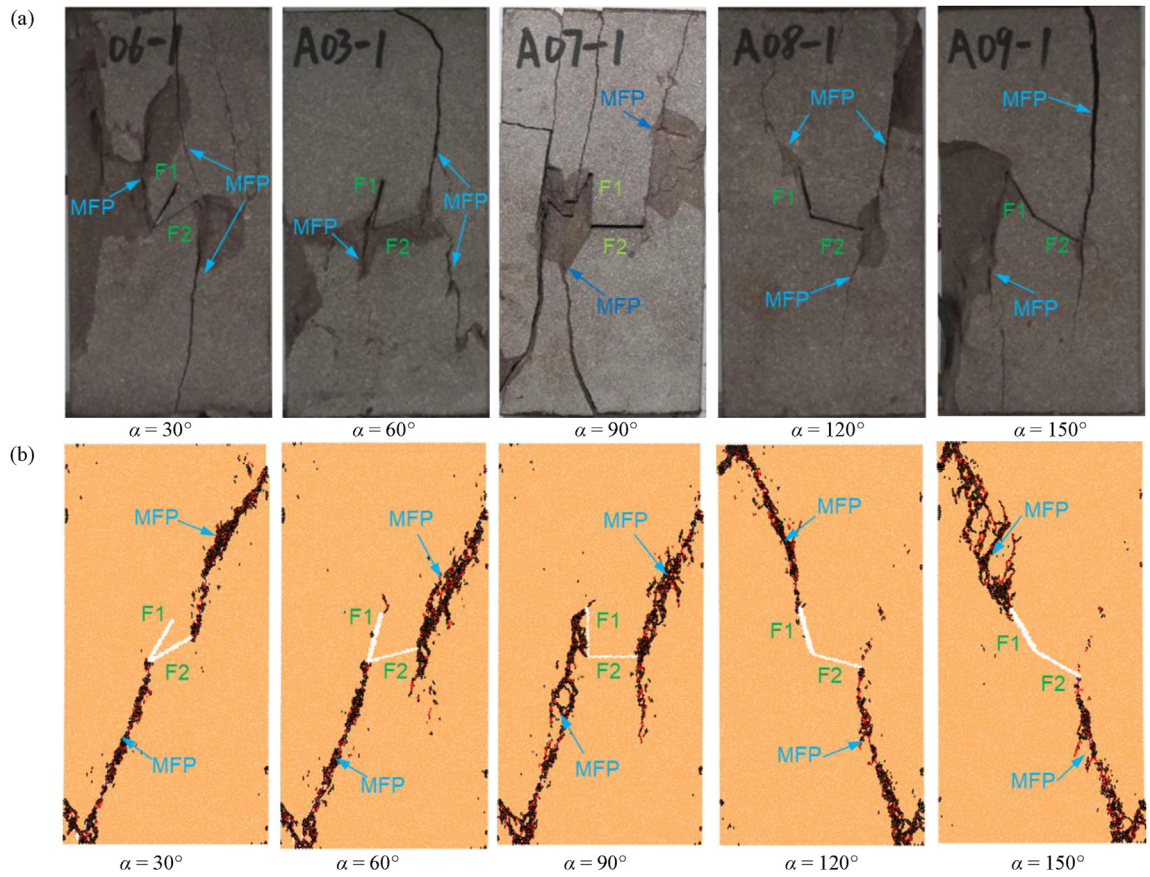

Fig. 6. Comparison between (a) experimental and (b) numerical failure modes of the sandstone samples containing intersecting fissures, with α varying from 30° to 150° at $\beta = 45°$ under uniaxial compression. Fissures 1 and 2 are represented by F1 and F2, respectively; MFP represents the main fracture plane.

experimental and numerical samples show consistent failure modes. As α ranges from 90° to 150°, the main fracture planes are formed at the outer tips of the two fissures, and the numerical sample has the same failure modes as the experimental sample for the same value of α. Both the simulated and experimental results reveal that as α increases, the positions of the main fracture planes change from the inner and outer tips of one fissure to the outer tips of two fissures. The failure modes of the numerical and experimental samples are quite similar and show a consistent change rule, with α varying from 30° to 150° under $\beta = 45°$. Surface spalling occurs on the left side of Fissure 1, wrapping the inner and outer tips of Fissure 1 in the experimental sample with $\alpha = 90°$. For the numerical sample with $\alpha = 90°$, microcracks are produced on the left side of Fissure 1, causing the coalescence of the inner and outer tips of Fissure 1. This phenomenon further demonstrates the accuracy of the PFC simulation.

The above verification results of the mechanical properties and failure modes indicate that the microscopic numerical parameters of sandstone obtained by trial and error can be used to study sandstone containing intersecting fissures.

4. Strength and deformation behaviours of sandstone containing intersecting fissures

Using the obtained microscopic numerical parameters of sandstone, further simulation was performed on sandstone containing intersecting fissures to assess the effects of intersecting angle α and orientation angle β on the mechanical behaviour of sandstone under uniaxial compression.

4.1. Axial stress–strain behaviours

Fig. 7 depicts the axial stress–strain curves of the samples at various values of α. The figure shows that there are three main stages in the stress–strain curve: the linear elastic stage, the nonlinear growth stage, and the postpeak drop stage. The curve does not exhibit compaction characteristics at the initial stage of loading. At the beginning of the loading, the curve enters the linear elastic stage, and the stress increases linearly with the strain. When the curve enters the nonlinear growth stage, the curve exhibits different degrees of stress fluctuation and drops due to crack propagation and coalescence. The stress reaches its peak at this stage. The post-peak drop stage follows the peak. The sample is completely destroyed at this stage, and the stress drops rapidly, demonstrating prominent brittleness characteristics. The curve with a higher peak point shows fewer stress drops and a smaller amplitude of the stress drop, or even no stress drops before the peak, such as sample 30–90. As the peak point of the curve decreases, more frequent stress drops occur in the curve. A great stress platform occurs after the peak point for samples 120-60 and 120-90. In addition, as the angle α increases, the angle β exerts a more significant impact on the peak point and slope of the elastic stage of the curves, especially when the angle α increases to 120° and 150°.

4.2. Mechanical parameters

The peak stress, peak strain, and average modulus of sandstone samples containing intersecting fissures under uniaxial compression with various angles α and β were obtained via simulations,

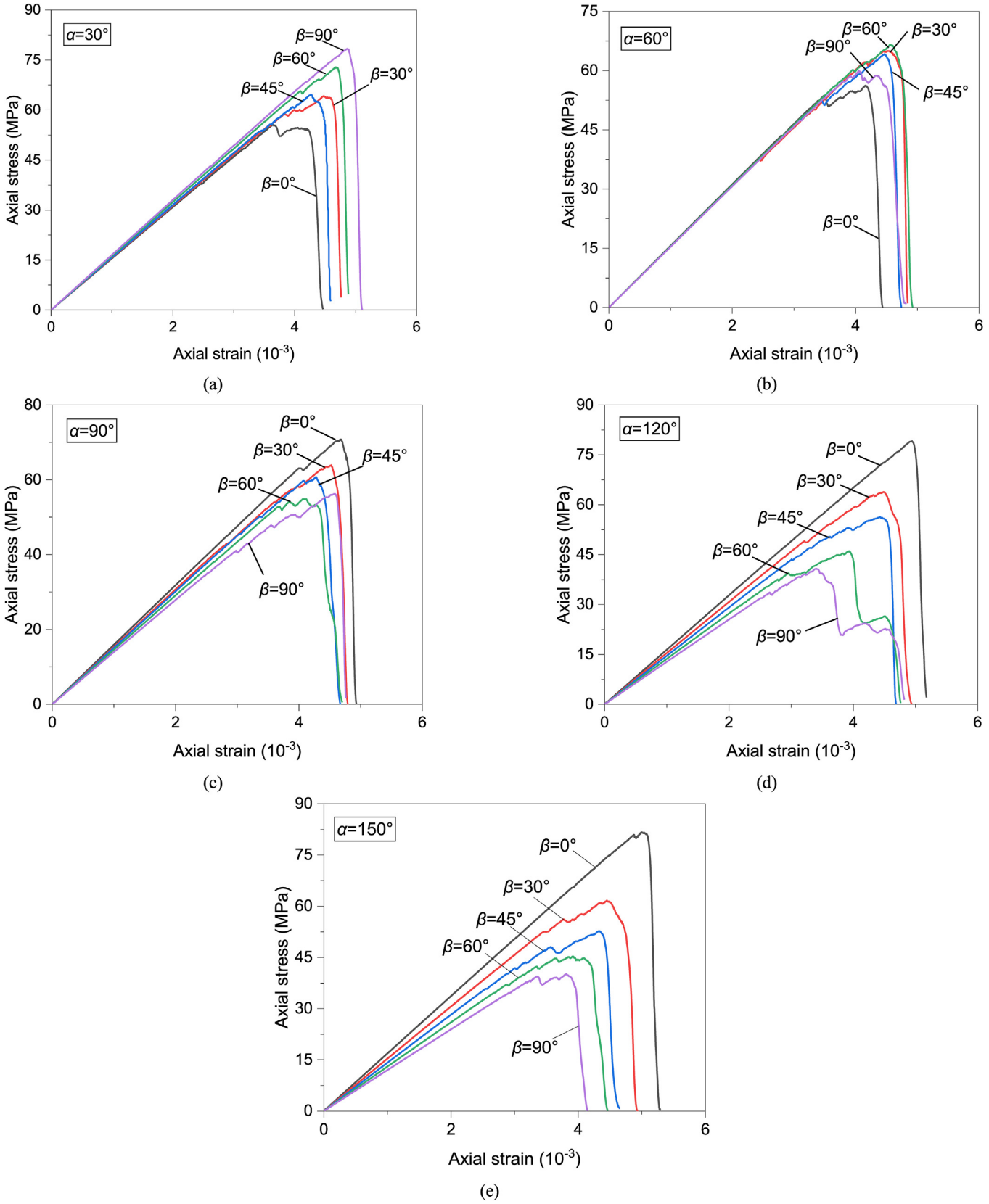

Fig. 7. Axial stress–strain curves of samples with intersecting fissures under uniaxial compression: (a) $\alpha = 30°$, (b) $\alpha = 60°$, (c) $\alpha = 90°$, (d) $\alpha = 120°$, and (e) $\alpha = 150°$.

Table 6
Peak stress at different α and β values.

β (°)	Peak stress (MPa)				
	$\alpha = 30°$	$\alpha = 60°$	$\alpha = 90°$	$\alpha = 120°$	$\alpha = 150°$
0	55.56 (0%)	56.2 (0%)	70.8 (0%)	79.14 (0%)	81.64 (0%)
30	64.18 (15.5%)	64.98 (15.6%)	63.92 (−9.7%)	63.88 (−19.3)	61.65 (−24.5%)
45	64.6 (16.3%)	64.17 (14.2%)	60.72 (−14.2%)	56.3 (−28.9%)	52.76 (−35.4%)
60	72.86 (31.1%)	66.51 (18.3%)	54.9 (−22.5%)	46.05 (−41.8%)	45.35 (−44.5%)
90	78.37 (41%)	59.95 (6.7%)	56.21 (−20.6%)	40.77 (−48.5%)	40.13 (−50.8%)

Note: Percentage changes relative to β of 0° are shown in parentheses.

Table 7
Average modulus at different α and β values.

β (°)	Average modulus (GPa)				
	$\alpha = 30°$	$\alpha = 60°$	$\alpha = 90°$	$\alpha = 120°$	$\alpha = 150°$
0	15.43 (0%)	15.59 (0%)	15.89 (0%)	16.36 (0%)	16.83 (0%)
30	15.59 (1%)	15.35 (−1.5%)	15.33 (−3.5%)	15.36 (−6.1%)	15.3 (−9.1%)
45	15.75 (2.1%)	15.38 (−1.3%)	15.06 (−5.2%)	14.52 (−11.2%)	14.1 (−16.2%)
60	16.17 (4.8%)	15.45 (−0.9%)	14.53 (−8.6%)	13.61 (−16.8%)	12.98(−22.9%)
90	16.51 (7%)	15.32 (−1.7%)	13.91 (−12.5%)	12.72 (−22.2%)	11.95 (−29%)

Note: Percentage changes relative to β of 0° are shown in parentheses.

Table 8
Revised peak strain at different α and β values.

β (°)	Revised peak strain (10^{-3})				
	$\alpha = 30°$	$\alpha = 60°$	$\alpha = 90°$	$\alpha = 120°$	$\alpha = 150°$
0	4.94 (0%)	5.46 (0%)	5.98 (0%)	6.24 (0%)	6.3 (0%)
30	5.78 (17.01%)	5.82 (6.66%)	5.82 (−2.61%)	5.78 (−7.4%)	5.75 (−8.69%)
45	5.56 (12.59%)	5.77 (5.68%)	5.58 (−6.71%)	5.73 (−8.23%)	5.63 (−10.67%)
60	5.97 (20.82%)	5.85 (7.24%)	5.37 (−10.28%)	5.23 (−16.18%)	5.22 (−17.16%)
90	6.16 (24.7%)	5.35 (−1.92%)	5.89 (−1.59%)	4.7 (−24.69%)	5.11 (−18.83%)

Note: Percentage changes relative to β of 0° are shown in parentheses.

which are given in Tables 6–8, respectively. The percentage changes of the values in each column with respect to β of 0° are shown in parentheses. These mechanical parameters are plotted in Fig. 8. The peak strain is the revised value obtained via the method of Yang et al. (2014). According to these tables and figures, the peak stress, average modulus, and peak strain show a similar variation trend with the changes in α and β. The variation in the mechanical parameters resembles a "moth" shape in 3D space. Taking the peak stress as an example, the analysis is described as follows:

(1) When β increases from 0° to 90°, the variation in the peak stress of the sample depends on angle α. The peak stresses gradually increase with an increase in β when $\alpha = 30°$, showing an increase of 41%. When the angle α is set at 60°, the peak stresses of the samples change within 18.35% with an increase in β. For α in the range of 90°–150°, the peak stress reduces with increasing β. When the angle α reaches 150°, the peak stress is reduced by 50.8% with an increase in β. The variation trend in the peak stress with an increase in β gradually changes, with α varying from 30° to 150°. In terms of the change amplitude, the peak stress is more sensitive to α values of 30° and 150°.

(2) When α increases from 30° to 150°, the change in the peak stress of the sample depends on the angle β. When β is less than 30°, the peak stress of the sample increases gradually with an increase in α. For $\beta = 30°$, all samples with different angles α have a close peak stress between 61.65 MPa and 64.98 MPa (Table 6). When β is between 45° and 90°, the peak stress gradually decreases as α increases, suggesting that there are two change rules in the peak stress with α, where $\beta = 30°$ is taken as the boundary. The peak stress is more sensitive to $\beta = 0°$ and 90°.

Since the axial loading is applied, the effective load-bearing width of the sample in the horizontal direction plays an important role. The mechanical parameters are positively related to the effective load-bearing width, defined as the sample width minus the projected length of the intersecting fissures in the horizontal direction, as shown in Fig. 9a. The variation in the effective load-bearing width of sandstone containing intersecting fissures with various α and β values is plotted in Fig. 9b. The variation surface of the effective load-bearing width in 3D space also has a "moth" shape. As a result, the mechanical parameters have a similar variation trend.

The average modulus has a consistent variation trend with the peak stress with changes in the angles α and β (see Table 7 and Fig. 8b). The overall trend of the revised peak strain with α and β also conforms to the above rules, except for individual points (see Table 8 and Fig. 8c), which will not be repeated here.

5. Failure characteristics of sandstone containing intersecting fissures

5.1. Crack initiation forms and stress

Crack initiation has received extensive attention, and its form reflects the dominant position of cracking. The crack initiation forms of sandstone samples containing intersecting fissures with

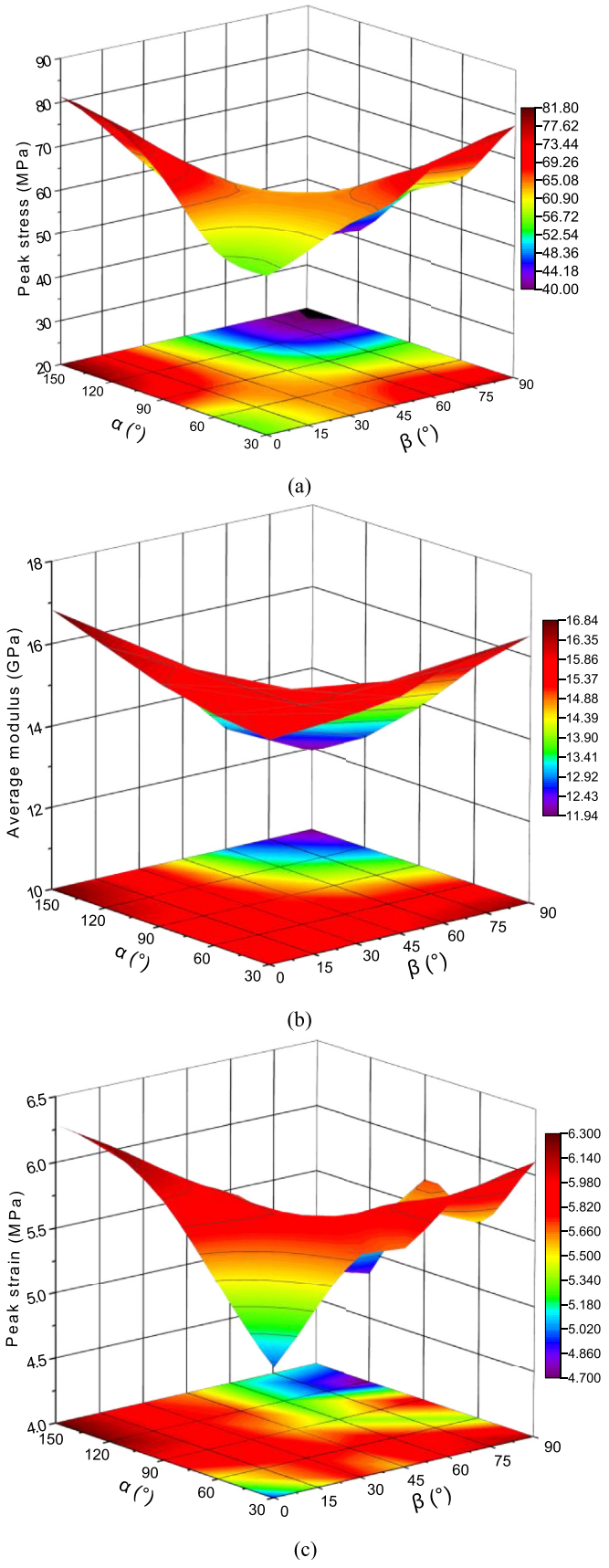

Fig. 8. Variations in the mechanical parameters of sandstone containing intersecting fissures with different α and β values, where (a), (b), and (c) show the variations in the peak stress, average modulus, and revised peak strain, respectively.

different intersecting angles α and distribution orientation angles β under uniaxial compression are shown in Fig. 10. When the number of microcracks in the sample reaches 1%–2% of the total number of microcracks in the final failure, crack initiation occurs. Some samples have crack initiation locations that are not exactly at the fissure tip, but are within a specific distance. From this figure, two crack initiation forms can be identified:

(1) Form 1: Crack initiation occurs at the inner tip of the fissures, and generally, the outer tip of Fissure 1 or 2 also initiates cracks. In most of these cases, cracks are initiated at the inner and outer tips of Fissure 2. In some of the samples, cracks are initiated at the inner and outer tips of Fissure 1, such as samples 30-0 and 90-0.
(2) Form 2: Crack initiations occur only at the outer tips of fissures, with no crack initiating at the inner tip. Generally, the outer tips of two fissures crack simultaneously, such as sample 150-30.

The relationship between the crack initiation forms and the angles α and β is shown in Fig. 11. The hollow purple squares indicate the presence of the form of an inner tip initiating crack (usually accompanied by one outer tip cracking simultaneously), and the hollow green circles indicate the presence of crack initiation only at the outer tips of the two fissures. From the figure, the crack initiation forms change from inner tip initiating cracks to outer tips initiating cracks with increasing α and β. This result demonstrates that the stress concentration effect of the inner tip weakens with increasing α and β, while the stress concentration effect on the outer tip of Fissure 1 is enhanced. As the figure shows, there is a boundary in the plane of intersecting angle α and distribution orientation angle β. When the cases are located at a zone below the boundary, the cracks on the inner tip initiate, usually accompanied by one outer tip cracking. When the cases are located at the zone above the boundary, crack initiations occur only at the outer tips of the two fissures, and usually, the cracks on the two outer tips initiate simultaneously.

The changes in the crack initiation stress of the samples with different α and β values are given in Table 9 and plotted in Fig. 12. We can see that the crack initiation stress shows a variation trend similar to the other mechanical parameters (such as the peak stress) of the samples, with varied angles α and β.

5.2. Final failure modes

The final failure modes of sandstone samples containing intersecting fissures with different α and β values are shown in Fig. 13. Under uniaxial compression, cracks are produced at the fissure tips and propagate and coalesce to form the main fracture planes. The main fracture plane is developed mainly by a tensile wing crack or an anti-wing crack at the fissure tip; however, not all fissure tips produce cracks and form the main fracture plane. According to the formation positions of the main fracture planes, two types of failure modes can be distinguished:

(1) Mode 1: The main fracture planes are created at the inner and outer tips of one fissure, such as samples 150-0, 90-30, and 30–60. In this mode, the main fracture plane from the outer tip may occur at the outer tip of Fissure 1 or Fissure 2. In most of these cases, the main fracture plane of the outer tip is created at the outer tip of Fissure 2. Cases for the creation of the main fracture plane at the outer tip of Fissure 1 require $\beta = 0°$ and $\alpha \leq 90°$, as shown in Fig. 13. Coalescence occurs between the outer tips of the two fissures in samples 30-0, 30-30, and 120-0.

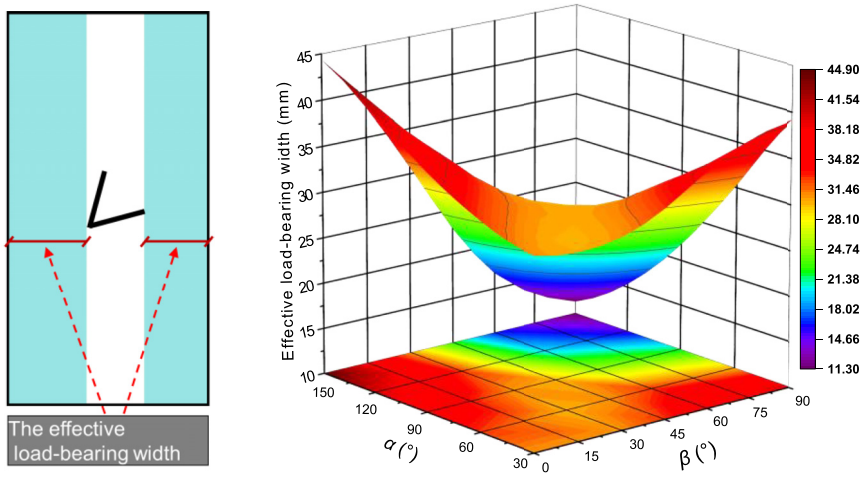

Fig. 9. (a) The effective load-bearing width of sandstone containing intersecting fissures and (b) its variation with different α and β values.

(2) Mode 2: The main fracture planes are created only at the outer tips of the two fissures rather than at the inner tip, such as samples 150-30, 90-45, and 30–90. Cracks are also produced at the inner tip in sample 90-45, which just form a coalescence with the main fracture plane from the outer tip of Fissure 1.

Based on the results of Figs. 13 and 14 shows the relationship between the formation positions of the main fracture planes and angles α and β. The red square represents that the main fracture planes are formed at the inner tip and one outer tip; the blue circle indicates that the main fracture planes are formed only from the outer tips of the two fissures. Clearly, there is also a boundary in the α–β plane. When the cases are located below the boundary, the main fracture planes occur at the inner tip and one outer tip. When the cases are located above the boundary, the main fracture planes occur only at the outer tips of the two fissures. This result can be explained as follows: as α and β increase, the stress concentration at the inner tip of the two fissures gradually weakens, while the stress concentration at the outer tip of another fissure gradually enhances. This mechanism is similar to that of variation in crack initiation forms.

From the results of Figs. 11 and 14, the crack initiation position corresponds to the final failure mode in most cases. However, the crack initiation forms of samples 60-60 and 120-30 do not correspond to their final failure modes, and the two samples are in the vicinity of the boundary, as shown in Fig. 14. These two samples show the following characteristics: crack initiation occurs at the outer tips of the two fissures, while a main fracture plane is formed at the inner tip when the samples fail entirely. This phenomenon concerns the crack evolution process, which will be analysed in detail in Section 5.3. This result implies that the boundaries of the crack initiation form and the failure mode are not the same, which will be shown in Section 6.

5.3. Two main types of the crack evolution process

There are two main types of crack evolution processes in sandstone samples containing intersecting fissures under uniaxial compression related to the initiation forms and the final failure modes. In the first type, the sample has a crack initiation form corresponding to the final failure mode. For this type, cracks initiate at the tips of the fissure, and the main fracture planes are formed at the cracked fissure tips by a tensile wing crack or an anti-wing crack.

In the second type of crack evolution process, the samples have a crack initiation form that does not correspond to the final failure mode, such as samples 60-60 and 120-30. Take sample 120-30 as an example for the analysis. The axial stress–strain curve and the fracture evolution process of sample 120-30 are depicted in Fig. 15. The capital letters in the samples correspond to the points at the axial stress–strain curve. When the stress is applied to point *A*, a tensile wing crack (T1) is generated at the outer tip of Fissure 2, and some microcracks are produced near the outer tip of Fissure 1. At point *B* ($\sigma_1 = 62.56$ MPa), a macroscopic tensile wing crack (T2) is observed at the outer tip of Fissure 1, while TI develops downward, and some discrete far-field cracks are formed at a certain distance from the outer tip of Fissure 2 on the right side of the sample. When the loading is continued to point *C* ($\sigma_1 = 63.12$ MPa), after the peak, the tensile wing crack (T2) at the outer tip of Fissure 1 propagates upward, and the tensile wing crack (T1) at the outer tip of Fissure 2 propagates farther downward, while another crack forms at the lower left corner of the sample. Subsequently, the stress drops sharply. From point *D* to point *F*, the stress drops from 54.92 MPa to 21.08 MPa, and the strain increases from 4.7×10^{-3} to 4.82×10^{-3}, with an increase of 2.55%. In such a short process, the main fracture plane is rapidly formed connecting the inner tip of fissures, while another main fracture plane is formed from the outer tip of Fissure 2. These two main fracture planes both belong to the anti-wing crack (A1 and A2). The tensile wing cracks (T1 and T2) generated from the outer tip of Fissures 1 and 2 are not fully propagated. In this type of crack evolution process, we found that the main fracture plane was not formed at the outer tip of Fissure 1, although a crack was initiated here at early loading. The main fracture plane at the inner tip was formed after the peak point. This process is relatively short, and the sign of the main fracture plane at the inner tip cannot be observed in the crack initiation form. Sample 60-60 has a similar crack propagation process. In addition, the relationship between the axial stress–strain curve and the crack evolution process indicates that the primary cause of sample instability and failure is the formation of the main fracture plane.

6. Fracture pattern determination

As shown in Sections 5.1 and 5.2, there are two boundaries in the plane of the intersecting angle α and the orientation angle β.

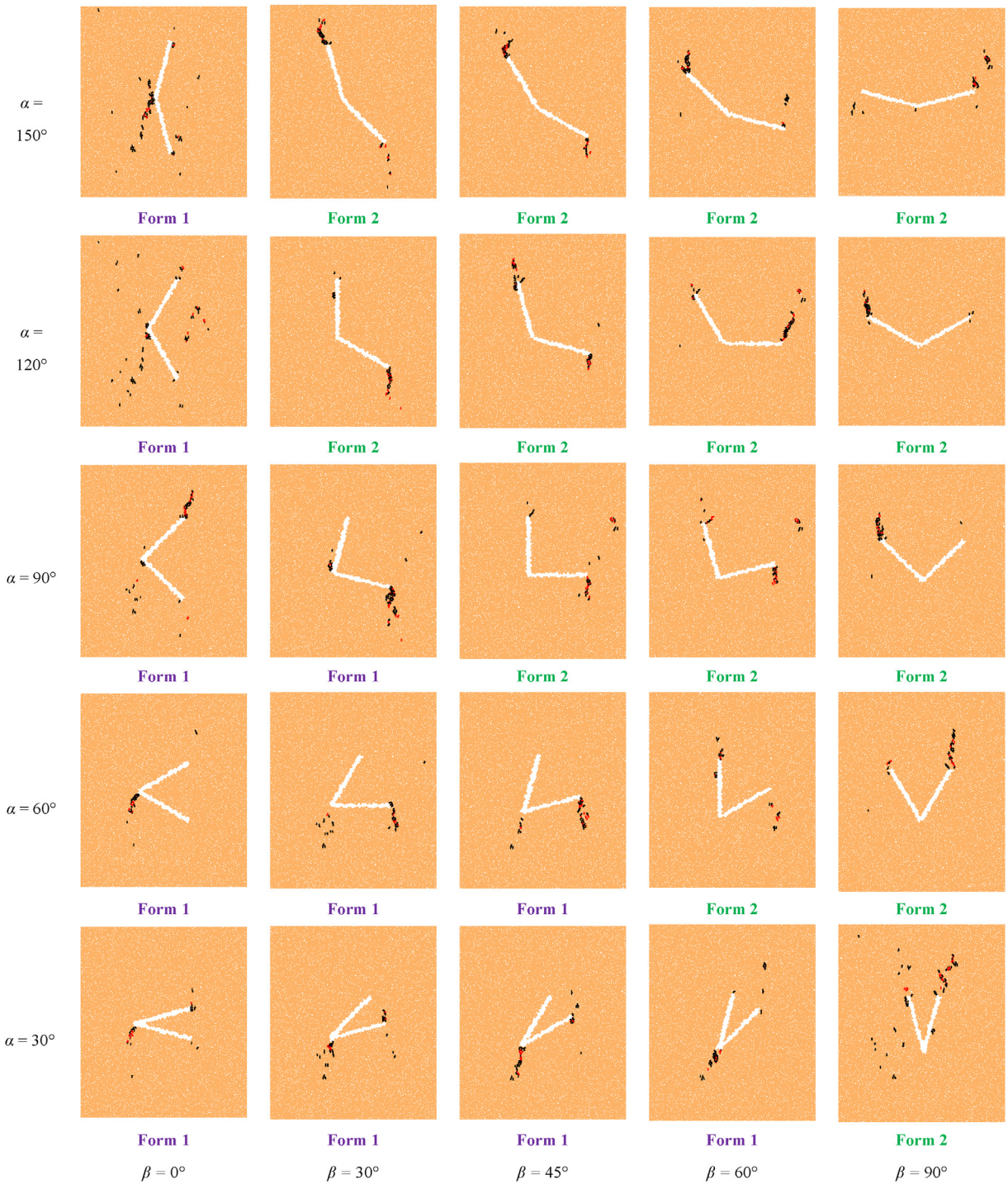

Fig. 10. Crack initiation forms of sandstone samples containing intersecting fissures versus different α and β values under uniaxial compression.

These two boundaries divide the crack initiation forms and failure modes of the sandstone containing intersecting fissures into two categories. This section studies the two boundaries and proposes approaches for determining the fracture pattern.

6.1. Approach for determining the crack initiation form

To accurately determine the equation of the boundary for the crack initiation form, extra 21 cases were simulated, with intersecting angles α of 165°, 150°, 135°, 120°, 105°, 90°, 75°, 60°, 45°, 30° and 15°. The corresponding distribution orientation angle β crosses the boundary, as shown in Fig. 16. The boundary is fitted with a straight line equation:

$$\alpha = I_1\beta + I_2 \tag{1}$$

where I_1 and I_2 are the material parameters of the sample. For the straight line fitted in this study, $I_1 = -1.86$ and $I_2 = 166.52$, with a

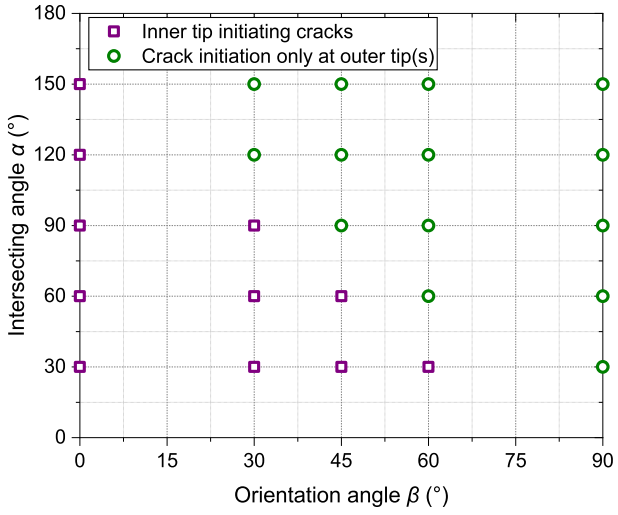

Fig. 11. The position of crack initiation of intersecting fissures with different α and β values. For the inner tip, initiating cracks are usually accompanied by one outer tip cracking simultaneously.

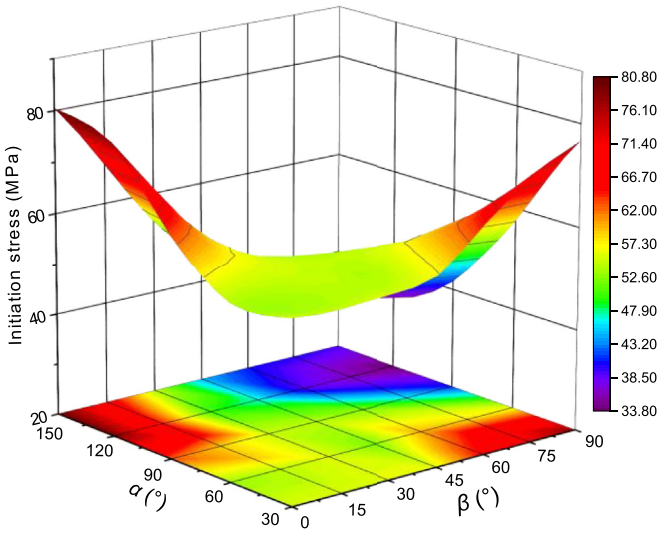

Fig. 12. Variation in the crack initiation stress of sandstone containing intersecting fissures with different α and β values.

fitting correlation coefficient of $R^2 = 0.94$. Based on the straight line in Fig. 16, an approach for determining the crack initiation form of sandstone containing intersecting fissures is proposed. For cases below the straight line, crack imitations occur at the inner and outer tips of one fissure. In most of these cases, crack initiations occur at the inner and outer tips of Fissure 2. However, for cases with $\beta = 0°$ and $\alpha \leq 90°$, crack initiations occur at the inner and outer tips of Fissure 1. In the cases above the straight line, crack initiations occur only at the two outer tips.

6.2. Approach for determining the failure mode

To accurately determine the boundary equation for the failure mode of sandstone containing intersecting fissures, extra 22 cases were simulated with intersecting angles α of 180°, 165°, 150°, 135°, 120°, 105°, 90°, 75°, 60°, 45°, 30°, and 15°. Two cases with $\alpha = 180°$ and an orientation angle β of other samples crossed the boundary, as shown in Fig. 17. The boundary is fitted by a cubic curve equation:

$$\alpha = E_1\beta^3 + E_2\beta^2 + E_3\beta + E_4 \quad (2)$$

where E_1, E_2, E_3 and E_4 are the material parameters of the sample. For the curve fitted in this study, $E_1 = 4 \times 10^{-4}$, $E_2 = -6.16 \times 10^{-2}$, $E_3 = 0.41$ and $E_4 = 172.63$, with a fitting correlation coefficient R^2 of 0.94. Based on the curve in Fig. 17, an approach for determining the failure mode of sandstone samples containing intersecting fissures is proposed. For the cases below the curve, the main fracture planes occur simultaneously from the inner and outer tips of one fissure. In most of these cases, the main fracture planes form from the inner and outer tips of Fissure 2; however, for cases with $\beta = 0°$ and $\alpha \leq 90°$, the main fracture planes form from the inner and outer tips of Fissure 1. In cases above the curve, the main fracture planes occur only at the two outer tips.

6.3. Approach for determining the crack evolution processes

The determination equation of the crack initiation form is different from that of the final failure mode. The determination equation of the crack initiation form is in a straight line, while the determination equation of the final failure mode is in a cubic curve, as shown in Fig. 18. When $\beta < 72°$, the determination equation of the failure mode is located above that of the crack initiation form, and when $\beta > 72°$, the two boundaries substantially coincide. The α–β plane is divided by the two determination equations into three zones, i.e. Z1, Z2 and Z3. Z1 is located below the straight line, Z2 is situated between the straight line and the curve, and Z3 is situated above the curve. For the cases within Z1 and Z3, the crack initiation positons correspond to the locations of the main fracture planes. However, the crack initiation forms of cases in Z2 do not correspond to its failure modes. For these cases, the crack is initiated at the outer tips rather than the inner tip in the crack initiation form, whereas the main fracture plane occurs at the inner tip in the final failure mode. Cases in this zone can be viewed as transitional samples between two failure modes. Based on the partition in the α–β plane, the crack evolution processes of sandstone containing intersecting fissures can be predicted and described as follows:

(1) For the cases in Z1 and Z3, the cracks initiate at the corresponding fissure tips and propagate stably. Finally, the main

Table 9
Crack initiation stress at different α and β values.

β (°)	Crack initiation stress (MPa)				
	$\alpha = 30°$	$\alpha = 60°$	$\alpha = 90°$	$\alpha = 120°$	$\alpha = 150°$
0	55.56 (0%)	53.26 (0%)	62.78 (0%)	79.04 (0%)	80.7 (0%)
30	55.95 (0.7%)	55.75 (4.7%)	55.07 (−12.3%)	50.11 (−36.6%)	54.28 (−32.7%)
45	55.97 (0.7%)	52.22 (−2%)	54.26 (−13.6%)	47.06 (−40.5%)	44.61 (−44.7%)
60	65.32 (17.6%)	59.94 (12.5%)	52.57 (−16.3%)	38.96 (−50.7%)	40.88 (−49.3%)
90	77.93 (40.3%)	56.74 (6.5%)	41.09 (−34.5%)	33.91 (−57.1%)	39.32 (−51.3%)

Note: Percentage changes relative to β of 0° are shown in parentheses.

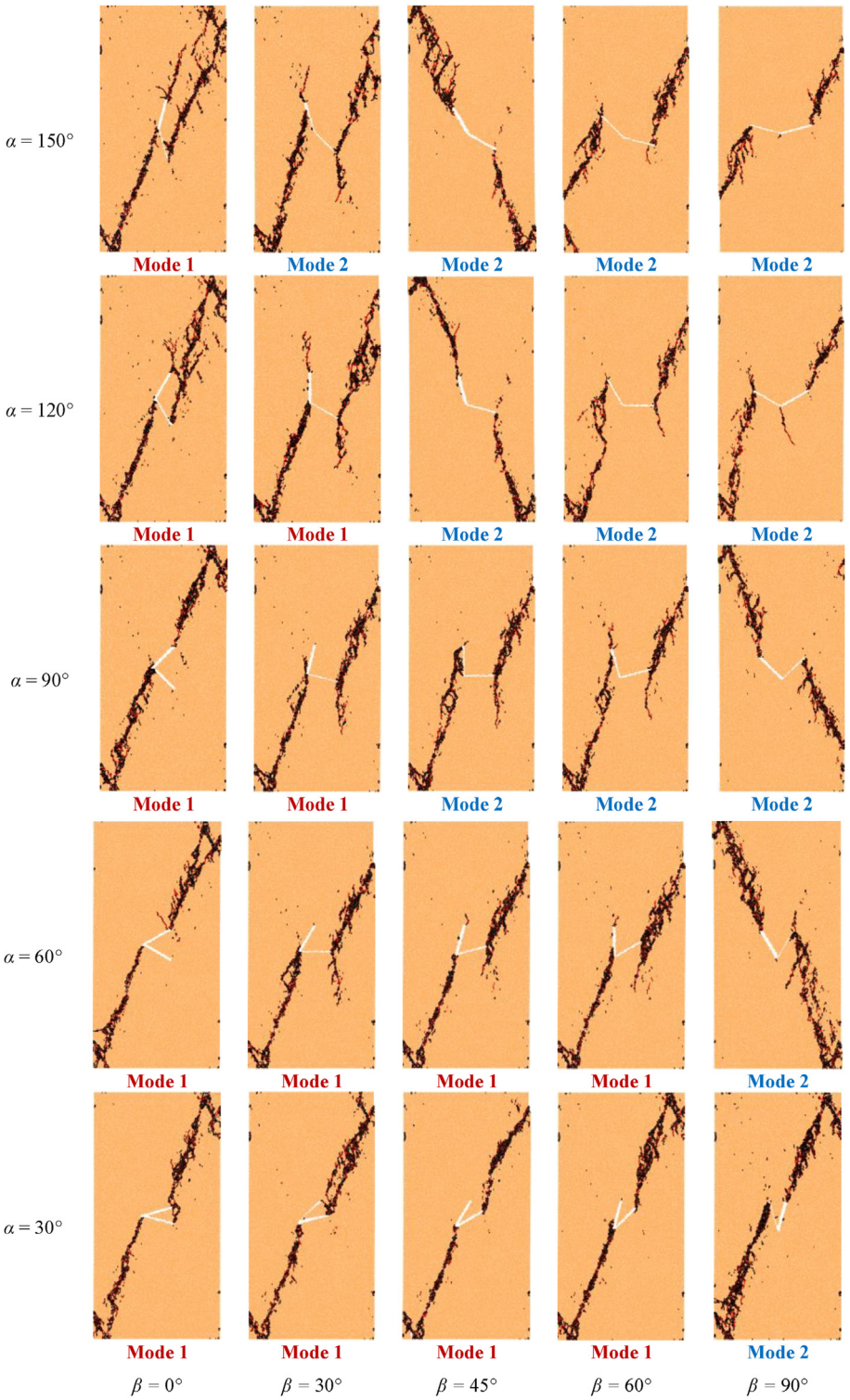

Fig. 13. The final failure modes of sandstone samples containing intersecting fissures with different α and β values under uniaxial compression.

fracture planes are formed at the cracked fissure tips. Tensile wing cracks or anti-wing cracks may propagate into the main fracture planes. This cracking process belongs to the first type, as described in Section 5.3.

(2) For the cases in Z2, the crack was not generated at the inner tip at the time of crack initiation. The main fracture plane is rapidly formed at the inner tip at the late stage (post-peak) of crack propagation, and the crack initiated at the outer tip of Fissure 1 cannot form the main fracture plane; however, a main fracture plane will be formed at the outer tip of Fissure 2. Similarly, the main fracture plane is propagated by a tensile wing crack or an anti-wing crack.

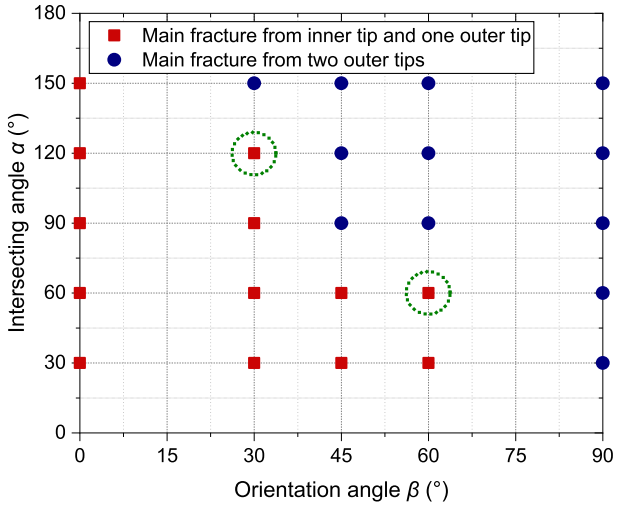

Fig. 14. The location of the main fracture planes in the sandstone sample containing intersecting fissures with different α and β values. The failure modes of the points (120-30 and 60-60) circled by the green dotted circle do not correspond to their crack initiation position (refer to Fig. 11).

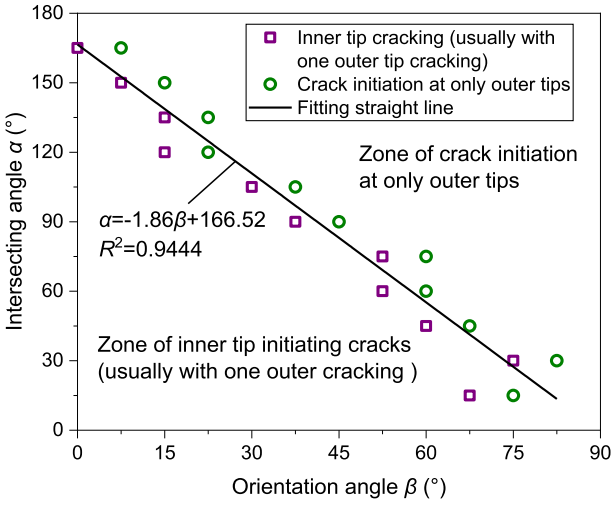

Fig. 16. Determination equation for the crack initiation forms and the partition of the α–β plane considering the determination equation.

Such a crack propagation process is similar to that of samples 120-30 and 60-60, belonging to the second type of cracking process, as described in Section 5.3.

The approaches for determining the crack initiation form and the failure mode provide a reference for quickly determining the cracking of rock containing intersecting fissures and can be used to predict and describe the fracture process with acceptable accuracy.

7. Conclusions

In this paper, the mechanical and failure properties of sandstone containing intersecting fissures under uniaxial compression were systematically studied via laboratory experiments and discrete

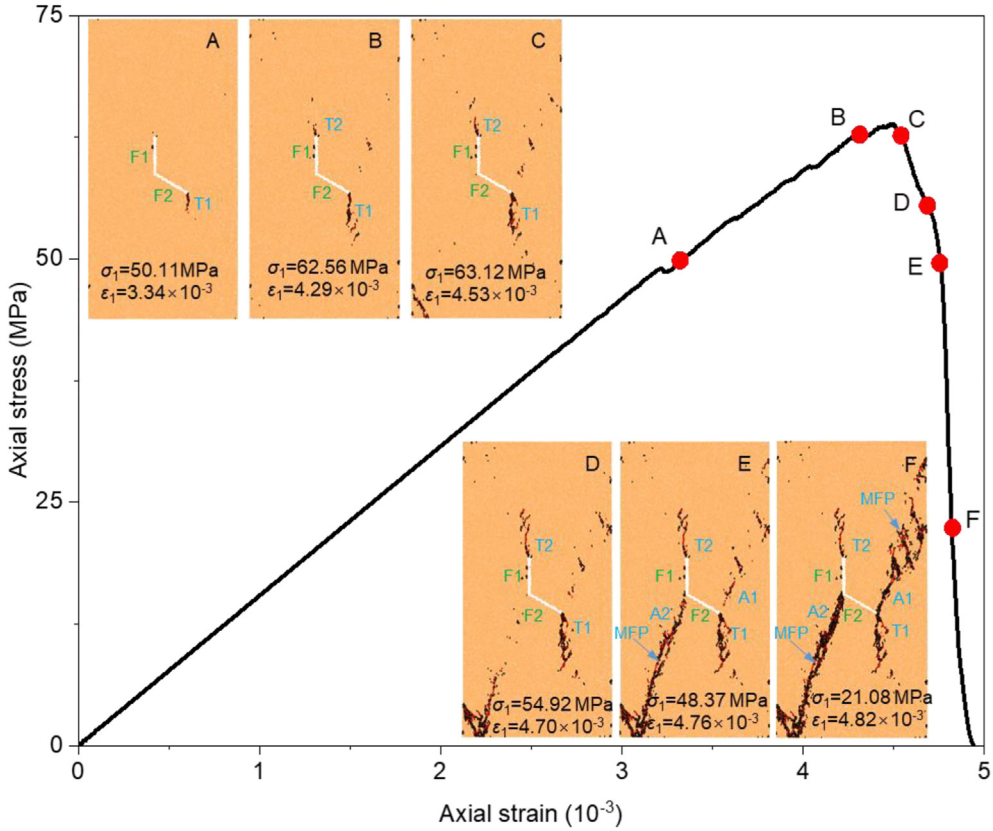

Fig. 15. The stress–strain curve and the crack evolution process of sample 120-30. The capital letters in the samples correspond to the points at the axial stress–strain curve. Fissures 1 and 2 are represented by F1 and F2, respectively; T and A represent the tensile wing cracks and anti-wing cracks, respectively; and MFP represents the main fracture plane.

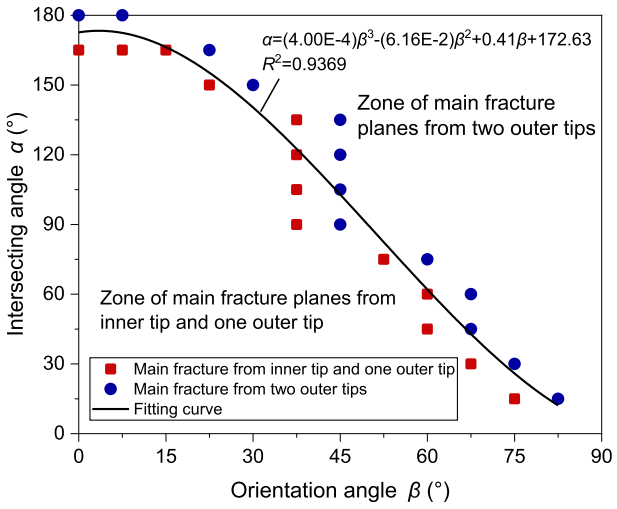

Fig. 17. Determination equation for the final failure modes and the partition of the α–β plane considering the determination equation.

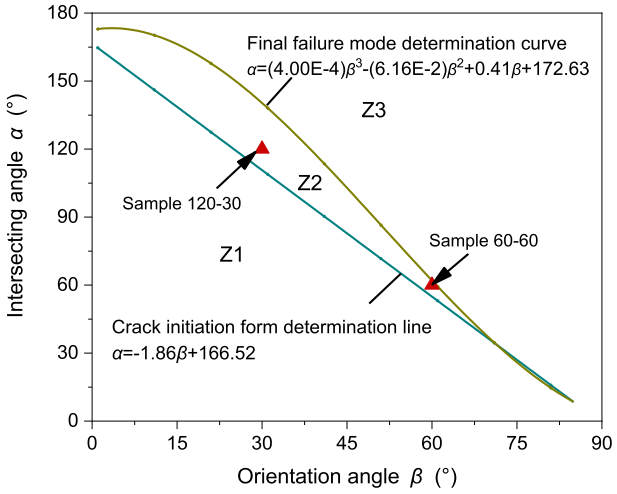

Fig. 18. Determination equations for the crack initiation forms and the final failure modes, and the partition in the α–β plane considering two determination equations.

element simulations. Two crack initiation forms, two failure modes, and two crack evolution process types were identified. Approaches for predicting the crack initiation form and the failure mode as well as the crack evolution process type were proposed. The following conclusions are drawn:

(1) The peak stress, average modulus, peak strain and crack initiation stress of sandstone samples containing intersecting fissures show similar variations with the changes in angles α and β. When $\alpha < 60°$, the mechanical parameters increase with increasing angle β. When $\alpha = 60°$, the mechanical parameters change little with the varied angle β. When α is large (at the range of 90°–150°), the mechanical parameters decrease with an increase in angle β. The variation surface of the mechanical parameter looks like a "moth" in the space of the α-β-mechanical parameters.

(2) Two crack initiation forms were identified: inner tip cracking (usually accompanied by one outer tip cracking) and only outer tips cracking. Based on the generation position of the main fracture planes, the final failure modes can be categorised into two modes. The first mode is the main fracture planes created at the inner tip and one outer tip, while the second mode is the main fracture planes formed at the two outer tips. The crack initiation form and final failure mode are determined by the intersecting angle α and the orientation angle β. Two main crack evolution processes of sandstone containing intersecting fissures under uniaxial compression were identified.

(3) Approaches for quickly determining the crack initiation form and the failure mode were proposed. The determination equation of the crack initiation form is in a straight line, while the determination equation of the failure mode is in a cubic curve. In the α–β plane, the determination equation for the failure mode is located above that for the crack initiation form. The two determination equations divide the α–β plane into three zones, where the zone between the two determination equations can be viewed as a transitional zone for two failure modes. The combination of determination equations for the crack initiation form and the failure mode can be used to predict the crack evolution. The approach for determining the crack evolution processes was hence proposed with high accuracy.

This paper investigated only the effects of the intersecting angle and the orientation angle of intersecting fissures on the mechanical and fracture properties of sandstone. To fully evaluate the fracture evolution mechanism of intersecting fissures, we will perform further research involving other parameters, such as the fissure length and opening.

Declaration of competing interest

The authors wish to confirm that there are no known conflicts of interest associated with this publication and there has been no significant financial support for this work that could have influenced its outcome.

Acknowledgments

This work was supported by the National Key R&D Program of China (Grant No. 2018YFC1504802), the National Natural Science Foundation of China (Grant No. 52074042) and the Basic Research and Frontier Exploration Project of Chongqing, China in 2018 (Grant No. cstc2018jcyjAX0453).

References

Afolagboye, L.O., He, J.M., Wang, S.J., 2017. Experimental study on cracking behaviour of moulded gypsum containing two non-parallel overlapping flaws under uniaxial compression. Acta Mech. Sin. 33 (2), 394–405.
Bocca, P., Carpinteri, A., Valente, S., 1990. Size effects in the mixed-mode crack-propagation - softening and snap-back analysis. Eng. Fract. Mech. 35 (1-3), 159–170.
Bobet, A., Einstein, H.H., 1998. Fracture coalescence in rock-type materials under uniaxial and biaxial compression. Int. J. Rock Mech. Min. Sci. 35 (7), 863–888.
Brideau, M.A., Yan, M., Stead, D., 2009. The role of tectonic damage and brittle rock fracture in the development of large rock slope failures. Geomorphology 103 (1), 30–49.
Bahaaddini, M., Hagan, P.C., Mitra, R., Hebblewhite, B.K., 2014. Scale effect on the shear behaviour of rock joints based on a numerical study. Eng. Geol. 181, 212–223.
Cao, P., Liu, T.Y., Pu, C.Z., Lin, H., 2015. Crack propagation and coalescence of brittle rock-like specimens with pre-existing cracks in compression. Eng. Geol. 187, 113–121.
Cao, R.H., Cao, P., Lin, H., Pu, C.Z., Ou, K., 2016. Mechanical behavior of brittle rock-like specimens with pre-existing fissures under uniaxial loading: experimental studies and particle mechanics approach. Rock Mech. Rock Eng. 49 (3), 763–783.
Cheng, C., Chen, X., Zhang, S.F., 2016. Multi-peak deformation behavior of jointed rock mass under uniaxial compression: Insight from particle flow modeling. Eng. Geol. 213, 25–45.

Castro-Filgueira, U., Alejano, L.R., Ivars, D.M., 2020. Particle flow code simulation of intact and fissured granitic rock samples. J. Rock Mech. Geotech. Eng. 12 (5), 960–974.
Cui, C., Gratchev, I., 2020. Effects of pre-existing cracks and infillings on strength of natural rocks - cases of sandstone, argillite and basalt. J. Rock Mech. Geotech. Eng. 12 (6), 1333–1338.
Donze, F.V., Richefeu, V., Magnier, S.A., 2009. Advances in discrete element method applied to soil rock and concrete mechanics. Electron. J. Geotech. Eng. 8, 1–44.
Feng, P., Dai, F., Liu, Y., Xu, N.W., Fan, P., 2018a. Effects of coupled static and dynamic strain rates on the mechanical behaviors of rock-like specimens containing preexisting fissures under uniaxial compression. Can. Geotech. J. 55, 640–652.
Feng, P., Dai, F., Liu, Y., Du, H.B., 2018b. Mechanical behaviors of rock-like specimens with two non-coplanar fissures subjected to coupled static-dynamic loads. Eng. Fract. Mech. 199, 692–704.
Feng, P., Dai, F., Liu, Y., Xu, N.W., Zhao, T., 2018c. Effects of strain rate on the mechanical and fracturing behaviors of rock-like specimens containing two unparallel fissures under uniaxial compression. Soil Dynam. Earthq. Eng. 110, 195–211.
Feng, P., Dai, F., Liu, Y., Xu, N.W., Du, H.B., 2019. Coupled effects of static-dynamic strain rates on the mechanical and fracturing behaviors of rock-like specimens containing two unparallel fissures. Eng. Fract. Mech. 207, 237–253.
Feng, P., Dai, F., Liu, Y., Xu, N.W., Zhao, T., 2020. Influence of two unparallel fissures on the mechanical behaviors of rock-like specimens subjected to uniaxial compression. Eur. J. Environ. Civ. En. 24 (10), 1643–1663.
Ghazvinian, A., Sarfarazi, V., Schubert, W., Blumel, M., 2012. A study of the failure mechanism of planar non-persistent open joints using PFC2D. Rock Mech. Rock Eng. 45 (5), 677–693.
Hosseini-Tehrani, P., Hosseini-Godarzi, A.R., Tavangar, M., 2005. Boundary element analysis of stress intensity factor K-I in some two-dimensional dynamic thermoelastic problems. Eng. Anal. Bound. Elem. 29 (3), 232–240.
Haeri, H., Shahriar, K., Marji, M.F., Moarefvand, P., 2014. Cracks coalescence mechanism and cracks propagation paths in rock-like specimens containing pre-existing random cracks under compression. J. Cent South Univ. 21 (6), 2404–2414.
Huang, D., Zhu, T.T., 2018. Experimental and numerical study on the strength and hybrid fracture of sandstone under tension-shear stress. Eng. Fract. Mech. 200, 387–400.
Han, G.S., Jing, H.W., Jiang, Y.J., Liu, R.C., Wu, J.Y., 2020. Effect of cyclic loading on the shear behaviours of both unfilled and infilled rough rock joints under constant normal stiffness conditions. Rock Mech. Rock Eng. 53 (1), 31–57.
Lee, H., Jeon, S., 2011. An experimental and numerical study of fracture coalescence in pre-cracked specimens under uniaxial compression. Int. J. Solid Struct. 48 (6), 979–999.
Liakas, S., O'Sullivan, C., Saroglou, C., 2017. Influence of heterogeneity on rock strength and stiffness using discrete element method and parallel bond model. J. Rock Mech. Geotech. Eng. 9 (4), 575–584.
Liu, Y., Dai, F., Fan, P.X., Xu, N.W., Dong, L., 2017. Experimental investigation of the influence of joint geometric configurations on the mechanical properties of intermittent jointed rock models under cyclic uniaxial compression. Rock Mech. Rock Eng. 50 (6), 1453–1471.
Liu, Y., Dai, F., Dong, L., Xu, N.W., Feng, P., 2018. Experimental investigation on the fatigue mechanical properties of intermittently jointed rock models under cyclic uniaxial compression with different loading parameters. Rock Mech. Rock Eng. 51 (1), 47–68.
Liu, X.R., Han, Y.F., Li, D.L., Tu, Y.L., Deng, Z.Y., Yu, C.T., Wu, X.C., 2019. Anti-pull mechanisms and weak interlayer parameter sensitivity analysis of tunnel-type anchorages in soft rock with underlying weak interlayers. Eng. Geol. 253, 123–136.
Manouchehrian, A., Sharifzadeh, M., Marji, M.F., Gholamnejad, J., 2014. A bonded particle model for analysis of the flaw orientation effect on crack propagation mechanism in brittle materials under compression. Arch. Civ. Mech. Eng. 14 (1), 40–52.
Potyondy, D.O., Cundall, P.A., 2004. A bonded-particle model for rock. Int. J. Rock Mech. Min. Sci. 41 (8), 1329–1364.
Prudencio, M., Jan, M.V., 2007. Strength and failure modes of rock mass models with non-persistent joints. Int. J. Rock Mech. Min. Sci. 44 (6), 890–902.
Park, C.H., Bobet, A., 2009. Crack coalescence in specimens with open and closed flaws: a comparison. Int. J. Rock Mech. Min. Sci. 46 (5), 819–829.
Rozycki, P., Moes, N., Bechet, E., Dubois, C., 2008. X-FEM explicit dynamics for constant strain elements to alleviate mesh constraints on internal or external boundaries. Comput. Methods Appl. Math. 197 (5), 349–363.
Romer, C., Ferentinou, M., 2019. Numerical investigations of rock bridge effect on open pit slope stability. J. Rock Mech. Geotech. Eng. 11 (6), 1184–1200.
Sagong, M., Bobet, A., 2002. Coalescence of multiple flaws in a rock-model material in uniaxial compression. Int. J. Rock Mech. Min. Sci. 39 (2), 229–241.
Scholtes, L., Donze, F.V., 2013. A DEM model for soft and hard rocks: role of grain interlocking on strength. J. Mech. Phys. Solid. 61 (2), 352–369.
Shi, C., Zhang, Q., Wang, S.N., 2018. Numerical Simulation Technology and Application with Particle Flow Code (PFC5.0). China Architecture & Building Press, Beijing, China (in Chinese).
Shaunik, D., Singh, M., 2019. Strength behaviour of a model rock intersected by non-persistent joint. J. Rock Mech. Geotech. Eng. 11 (6), 1243–1255.
Sun, W.B., Du, H.Q., Zhou, F., Shao, J.L., 2019. Experimental study of crack propagation of rock-like specimens containing conjugate fractures. Geomech. Eng. 17 (4), 323–331.
Wong, R.H.C., Chau, K.T., 1998. Crack coalescence in a rock-like material containing two cracks. Int. J. Rock Mech. Min. Sci. 35 (2), 147–164.
Wong, L.N.Y., Einstein, H.H., 2009a. Systematic evaluation of cracking behavior in specimens containing single flaws under uniaxial compression. Int. J. Rock Mech. Min. Sci. 46 (2), 239–249.
Wong, L.N.Y., Einstein, H.H., 2009b. Crack coalescence in molded gypsum and carrara marble: part 1. macroscopic observations and interpretation. Rock Mech. Rock Eng. 42 (3), 475–511.
Wong, L.N.Y., Einstein, H.H., 2009c. Crack coalescence in molded gypsum and Carrara marble: part 2-microscopic observations and interpretation. Rock Mech. Rock Eng. 42 (3), 513–545.
Wong, L.N.Y., Li, H.Q., 2013. Numerical study on coalescence of two pre-existing coplanar flaws in rock. Int. J. Solid Struct. 50 (22-23), 3685–3706.
Wang, Y.T., Zhou, X.P., Shou, Y.D., 2017. The modeling of crack propagation and coalescence in rocks under uniaxial compression using the novel conjugated bond-based peridynamics. Int. J. Mech. Sci. 128, 614–643.
Wang, Y.T., Zhou, X.P., Kou, M.M., 2019. Three-dimensional numerical study on the failure characteristics of intermittent fissures under compressive-shear loads. Acta Geotech 14 (4), 1161–1193.
Xiong, F., Jing, H.W., Su, H.J., Du, M.R., Yin, Q., Han, G.S., 2017. Strength and fracture behaviors of sandstone samples containing intersect fissures under uniaxial compression. J. China Coal Soc. 42 (4), 886–895 (in Chinese).
Xiong, F., Liu, X.R., Lin, G.Y., Zhou, X.H., Liu, D.S., Xu, B., Han, Y.F., He, C.M., Wang, Z.J., 2021. Experimental and numerical study on strength and deformation behaviors of sandstone with intersecting flaws. Geomech. Eng. 26 (6), 565–579.
Xu, J., Li, Z.X., 2019. Crack propagation and coalescence of step-path failure in rocks. Rock Mech. Rock Eng. 52 (4), 965–979.
Yang, S.Q., Jing, H.W., 2011. Strength failure and crack coalescence behavior of brittle sandstone samples containing a single fissure under uniaxial compression. Int. J. Fract. 168 (2), 227–250.
Yang, S.Q., Huang, Y.H., Jing, H.W., Liu, X.R., 2014. Discrete element modeling on fracture coalescence behavior of red sandstone containing two unparallel fissures under uniaxial compression. Eng. Geol. 178, 28–48.
Yang, S.Q., Huang, Y.H., Ranjith, P.G., Jiao, Y.Y., Ji, J., 2015. Discrete element modeling on the crack evolution behavior of brittle sandstone containing three fissures under uniaxial compression. Acta Mech. Sin. 31 (6), 871–889.
Yang, S.Q., Huang, Y.H., Tian, W.L., Zhu, J.B., 2017. An experimental investigation on strength, deformation and crack evolution behavior of sandstone containing two oval flaws under uniaxial compression. Eng. Geol. 217, 35–48.
Yin, Q., Jing, H.W., Su, H.J., 2018. Investigation on mechanical behavior and crack coalescence of sandstone specimens containing fissure-hole combined flaws under uniaxial compression. Geosci. J. 22 (5), 825–842.
Zhang, X.P., Wong, L.N.Y., 2012. Cracking processes in rock-like material containing a single flaw under uniaxial compression: a numerical study based on parallel bonded-particle model approach. Rock Mech. Rock Eng. 45 (5), 711–737.
Zhang, X.P., Wong, L.N.Y., 2013. Loading rate effects on cracking behavior of flaw-contained specimens under uniaxial compression. Int. J. Fract. 180 (1), 93–110.
Zhang, X.P., Zhang, Q., Wu, S.C., 2017. Acoustic emission characteristics of the rock-like material containing a single flaw under different compressive loading rates. Comput. Geotech. 83, 83–97.
Zhang, J.Z., Zhou, X.P., Zhou, L.S., Berto, F., 2019. Progressive failure of brittle rocks with non-isometric flaws: Insights from acousto-optic-mechanical (AOM) data. Fatigue Fract Eng M 42 (8), 1787–1802.
Zhang, S.G., Chen, L., Lu, P.P., Liu, W.B., 2021. Discussion on failure mechanism and strength criterion of sandstone based on particle discrete element method. KSCE J. Civ. Eng. 25 (6), 2314–2333.
Zhao, Z.H., Zhou, D., 2016. Mechanical properties and failure modes of rock samples with grout-infilled flaws: a particle mechanics modeling. J. Nat. Gas Sci. Eng. 34, 702–715.
Zhou, Y., Zhao, D.J., Li, B., Wang, H.Y., Tang, Q.Q., Zhang, Z.Z., 2021. Fatigue damage mechanism and deformation behaviour of granite under ultrahigh-frequency cyclic loading conditions. Rock Mech. Rock Eng. 54 (9), 4723–4739.
Zhu, T.T., Chen, J.X., Huang, D., Luo, Y.B., Li, Y., Xu, L.F., 2021. A dem-based approach for modeling the damage of rock under freeze-thaw cycles. Rock Mech. Rock Eng. 54 (6), 2843–2858.

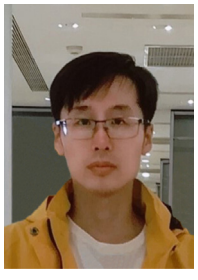

Fei Xiong is a PhD candidate at the School of Civil Engineering, Chongqing University, China. He obtained his BSc and MSc degrees from China University of Mining and Technology in 2014 and 2017, respectively. His current research interests include the mechanical behavior of fractured rock, the stability of rock slopes, and shield tunnel excavation. He has participated in several national projects related to geotechnical (underground) engineering.